Science

AAAS

Midbody Targeting of the ESCRT Machinery by a Noncanonical Coiled Coil in CEP55

Hyung Ho Lee, *et al.*
Science **322**, 576 (2008);
DOI: 10.1126/science.1162042

sion energies at which experiments were done, the experimental Cl/Cl* + H_2 DCSs were scaled to the theoretical CW values by means of a single multiplicative factor.

The reactive backward DCS for the BO-allowed Cl-atom reaction increases much more rapidly with increasing collision energy than that for the BO-forbidden reaction of Cl*. This was the prediction of our earlier scattering calculations (5). The energy dependence of the ratio of the backward DCSs for the Cl and Cl* reactions is shown in Fig. 4B. As can be seen, agreement with the predictions of quantum-scattering calculations on both PESs is almost always within the experimental uncertainty limits. Only at the lowest collision energy studied here, ~ 4.2 kcal/mol, is the excited spin-orbit state more reactive than the ground spin-orbit state.

The excellent overall agreement between our molecular beam experiments and the results of quantum-reactive scattering calculations on two sets of ab initio PESs indicates that the theoretical formulation includes correctly the essential physics governing the nonadiabatic processes of importance in the Cl + H_2 reaction. The degree of agreement, both for this and the F/F*+D_2 reaction (11), demonstrates that we can now attain the same level of accuracy in the theoretical modeling of triatomic reactions involving multiple PESs as has been achieved previously for reactions in which only one PES is included (6, 10, 30, 31). Ultimately, the success attained here should en-

courage similarly detailed experimental-theoretical investigations of non-BO effects in more complex chemical reactions (32, 33).

References and Notes

1. T. C. Allison et al., in Gas-Phase Chemical Reaction Systems: Experiments and Models 100 Years After Max Bodenstein, J. Wolfrum, H.-R. Volpp, R. Rannacher, J. Warnatz, Eds. (Springer, Heidelberg, Germany, 1996), pp. 111–124.
2. M. Alagia et al., Science 273, 1519 (1996).
3. P. Casavecchia, Rep. Prog. Phys. 63, 355 (2000).
4. K. J. Laidler, Chemical Kinetics (Harper and Row, New York, 1987), pp. 14, 288–298.
5. M. H. Alexander, G. Capecchi, H.-J. Werner, Science 296, 715 (2002).
6. D. Skouteris et al., Science 286, 1713 (1999).
7. N. Balucani et al., Phys. Rev. Lett. 91, 013201 (2003).
8. E. Garand, J. Zhou, D. E. Manolopoulos, M. H. Alexander, D. M. Neumark, Science 319, 72 (2008).
9. D. E. Manolopoulos et al., Science 262, 1852 (1993).
10. M. Qiu et al., Science 311, 1440 (2006).
11. L. Che et al., Science 317, 1061 (2007).
12. M. H. Alexander, G. Capecchi, H.-J. Werner, Faraday Discuss. Chem. Soc. 127, 59 (2004).
13. J. M. Bowman, Science 319, 40 (2008).
14. P. J. Dagdigian, M. L. Campbell, Chem. Rev. 87, 1 (1987).
15. G. Li, H.-J. Werner, F. Lique, M. H. Alexander, J. Chem. Phys. 127, 174302 (2007).
16. W. Bian, H.-J. Werner, J. Chem. Phys. 112, 220 (2000).
17. H.-J. Werner, M. Kallay, J. Gauss, J. Chem. Phys. 128, 034305 (2008).
18. S. H. Lee, L.-H. Lai, K. Liu, H. Chang, J. Chem. Phys. 110, 8229 (1999).
19. F. Dong, S.-H. Lee, K. Liu, J. Chem. Phys. 115, 1197 (2001).
20. B. F. Parsons, K. E. Strecker, D. W. Chandler, Eur. Phys. J. 38, 15 (2006).
21. M. H. Alexander, J. Kłos, D. E. Manolopoulos, J. Chem. Phys. 128, 084312 (2008).
22. L. Schnieder, K. Seekamp-Rahn, E. Wrede, K. H. Welge, J. Chem. Phys. 107, 6175 (1997).
23. G. Capecchi, H.-J. Werner, Phys. Chem. Chem. Phys. 6, 4975 (2004).
24. M. Qiu et al., Rev. Sci. Instrum. 76, 083107 (2005).
25. Methods are available as supporting material on Science Online. See fig. S1 for the REMPI spectrum of the Cl and Cl* atoms, fig. S2 for a comparison of the lowest CW and JX PES in collinear geometry, and fig. S3 for a comparison of the DCSs predicted by the simulations on the CW and JX PESs.
26. M. H. Alexander, D. E. Manolopoulos, H. J. Werner, J. Chem. Phys. 113, 11084 (2000).
27. M. H. Alexander, Y.-R. Tzeng, D. Skouteris, in Chemical Reaction Dynamics, G. Lendvay, A. Laganá, Eds. (Kluwer, Amsterdam, 2004), pp. 45–65.
28. K. Stark, H.-J. Werner, J. Chem. Phys. 104, 6515 (1996).
29. D. Skouteris et al., J. Chem. Phys. 114, 10662 (2001).
30. S. Althorpe et al., Nature 416, 67 (2002).
31. F. J. Aoiz, L. Bañares, V. J. Herrero, Int. Rev. Phys. Chem. 24, 119 (2005).
32. W. Hu, G. Lendvay, B. Maiti, G. C. Schatz, J. Phys. Chem. A 112, 2093 (2008).
33. P. Casavecchia et al., J. Phys. Chem. A 109, 3527 (2005).
34. X.Y. and D.H.Z. were supported by the Chinese Academy of Sciences, the National Natural Science Foundation of China, and the Ministry of Science and Technology of China. D.X. was supported by the National Natural Science Foundation of China (20533060 and 20725312). P.C. is grateful to X.Y. and the Dalian Institute of Chemical Physics for a visiting professorship. H.J.W. is grateful to the German Fonds der Chemischen Industrie for financial support.

Midbody Targeting of the ESCRT Machinery by a Noncanonical Coiled Coil in CEP55

Hyung Ho Lee,[1] Natalie Elia,[2] Rodolfo Ghirlando,[1] Jennifer Lippincott-Schwartz,[2] James H. Hurley[1]*

The ESCRT (endosomal sorting complex required for transport) machinery is required for the scission of membrane necks in processes including the budding of HIV-1 and cytokinesis. An essential step in cytokinesis is recruitment of the ESCRT-I complex and the ESCRT-associated protein ALIX to the midbody (the structure that tethers two daughter cells) by the protein CEP55. Biochemical experiments show that peptides from ALIX and the ESCRT-I subunit TSG101 compete for binding to the ESCRT- and ALIX-binding region (EABR) of CEP55. We solved the crystal structure of EABR bound to an ALIX peptide at a resolution of 2.0 angstroms. The structure shows that EABR forms an aberrant dimeric parallel coiled coil. Bulky and charged residues at the interface of the two central heptad repeats create asymmetry and a single binding site for an ALIX or TSG101 peptide. Both ALIX and ESCRT-I are required for cytokinesis, which suggests that multiple CEP55 dimers are required for function.

Cytokinesis, the division of the cytoplasm, is the final step of the M phase of the cell cycle. Cytokinesis begins with the formation of the contractile ring, which drives the growth of the cleavage furrow. Vesicle trafficking components, including the exocyst complex and SNAREs (soluble N-ethylmaleimide–sensitive factor attachment protein receptors), deliver the additional membrane needed for the cleavage furrow to grow (1–3). When the extension of the furrow ends, the contractile ring disassembles, and a structure known as the midbody remains as the final tether between the two daughter cells. The last step in cytokinesis, the cleavage of the plasma membrane at the midbody, is referred to as abscission. The mechanism of abscission became clearer with the discovery that the midbody protein CEP55 (4–6) recruits two key components of

the ESCRT machinery (7–11): the ESCRT-I complex and ALIX (12, 13). The role of ALIX and ESCRT-I in abscission appears to be recruitment of ESCRT-III subunits, which are required for normal midbody morphology (14) and are widely believed to have a membrane scission activity (15).

Deletion analysis of ALIX mapped the interaction with CEP55 to a putative unstructured Pro-rich sequence near its C terminus (12, 13). Similarly, the TSG101 subunit of ESCRT-I interacts via an unstructured linker between its ubiquitin-binding UEV domain and the region that forms the core complex with other ESCRT-I subunits (12, 13). CEP55 is a predominantly coiled-coil protein that otherwise lacks familiar protein-protein interaction domains. The predicted coiled coil of CEP55 is interrupted near the middle by a ~60-residue region that has been suggested to serve as a hinge between the N- and C-terminal coiled-coil regions (13). Remarkably, this putative hinge region is also the locus for binding to the putative unstructured Pro-rich regions of ALIX and TSG101. Because it is very unusual for two unstructured regions from two different proteins to drive spe-

[1]Laboratory of Molecular Biology, National Institute of Diabetes and Digestive and Kidney Diseases, Bethesda, MD 20892, USA. [2]Cell Biology and Metabolism Branch, National Institute of Child Health and Human Development, Bethesda, MD 20892, USA.

*To whom correspondence should be addressed. E-mail: hurley@helix.nih.gov

Fig. 1. The CEP55 ESCRT- and ALIX-binding region (EABR) and its interactions. (**A**) Predicted coiled-coil regions (yellow) and the EABR of CEP55 (blue). The region designated EABR corresponds to the region formerly suggested to be a hinge between the N- and C-terminal coiled coils (13). (**B**) CEP55 binding sequences of ALIX and the ESCRT-I subunit TSG101. Conserved residues are highlighted in light green; residues shown to be functionally important in ALIX are in bold red type (21). (**C**) Pull-down of CEP55-EABR by the GST-ALIX fragment shown, in the presence of the indicated amounts of TSG101 peptide competitor. (**D**) Isothermal titration calorimetry (ITC) of ALIX peptide into CEP55-EABR solution. (**E**) ITC of TSG101 peptide into CEP55-EABR solution.
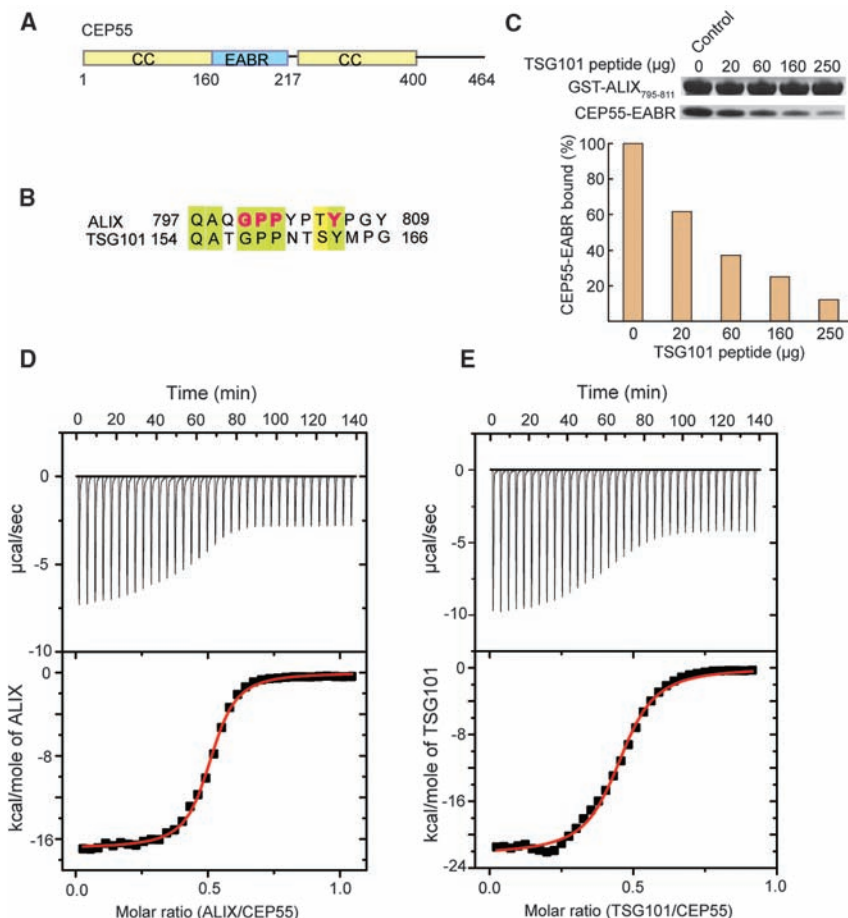

Fig. 2. Structure of the noncanonical CEP55-EABR coiled coil and its complex with ALIX. (**A**) The overall structure of the CEP55-EABR homodimer (green and blue ribbons) in complex with the ALIX peptide (stick model: carbon, orange; oxygen, red; nitrogen, blue). (**B**) Helical wheel analysis of the six heptad repeats of the EABR coiled coil (21). (**C**) Charge repulsion between Asp[188], Arg[191], and Glu[192] pairs in the homodimer creates asymmetry in the coiled coil and interactions with the ALIX peptide. (**D**) Overview and close-ups of selected regions of the CEP55 surface (carbon, green; oxygen, red; nitrogen, blue), with the ALIX peptide colored as in (A). (**E** to **G**) Molecular interactions in the complex shown in detail and colored as in (A).
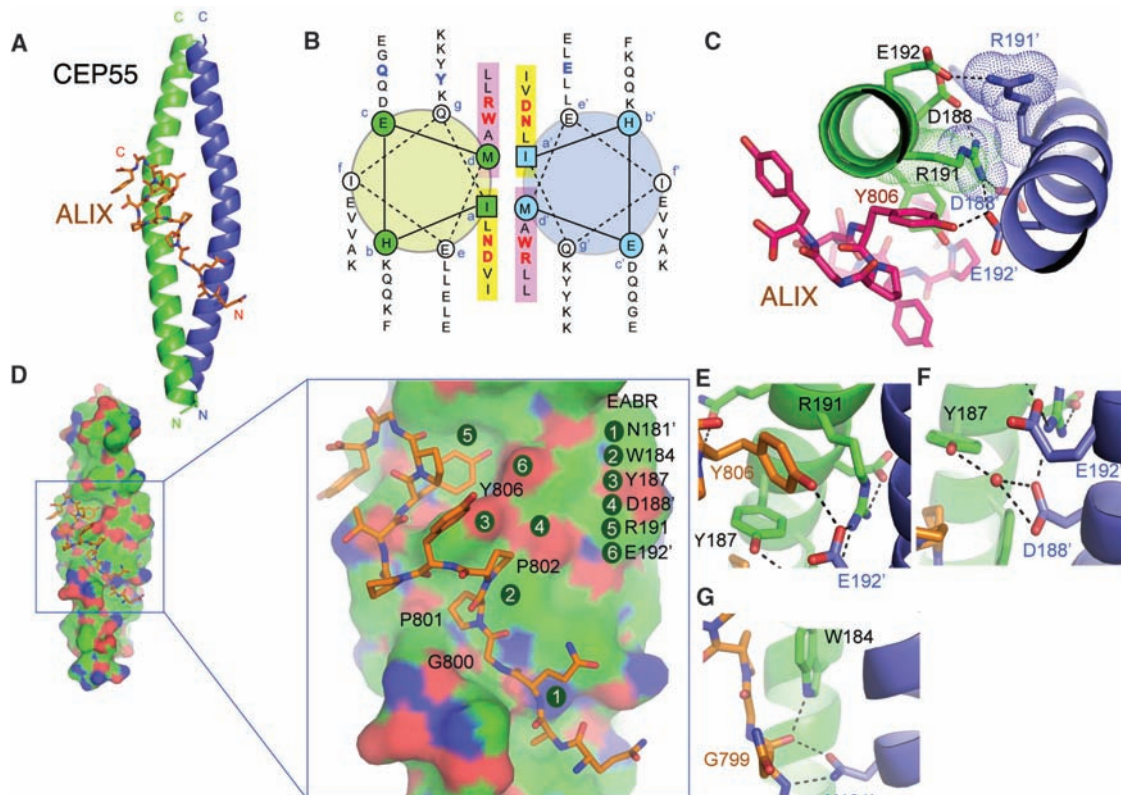
cific contacts between them, we pursued a more detailed deletion analysis (fig. S1) with the aim of characterizing binding constants, stoichiometry, and the structural basis of the interaction.

The CEP55 fragment EABR containing residues 160 to 217 (Fig. 1A and fig. S1) bound to a 13-residue peptide based on the Pro-rich sequence of ALIX (residues 797 to 809) (Fig. 1B) with a dissociation constant $K_d = 1$ μM and a stoichiometry of 2:1 (Fig. 1D). The EABR bound to the related TSG101 peptide (residues 154 to 166) with essentially the same affinity and stoichiometry (Fig. 1E). Various CEP55-EABR:peptide stoichiometric mixtures were subjected to analytical ultracentrifugation (figs. S2 to S4). A 2:1 EABR:ALIX mixture showed the presence of a single complex, whereas all mixtures having a higher proportion of peptide resulted in the 2:1

complex as well as excess free peptide. Similarly, a peptide derived from the Pro-rich region of TSG101 formed a 2:1 CEP55:peptide complex (fig. S2). When the TSG101 peptide was added to a preformed 2:1 CEP55:ALIX peptide complex, a peak corresponding to the equivalent amount of uncomplexed peptide was formed, which suggests that TSG101 and ALIX compete for the same site (fig. S2, bottom panel). Competitive binding experiments (Fig. 1C) confirmed that the two peptides interact with the same site.

To gain further insight into the structural organization of ESCRTs at the midbody, we determined the 2.0 Å resolution structure of CEP55-EABR bound to the ALIX peptide (Fig. 2A, fig. S5, and table S1). The EABR forms a parallel coiled coil over its entire length, comprising a total of six heptad repeats (Fig. 2B). In

the two heptad repeats closest to the N and C termini, respectively, there is canonical hydrophobic packing between the two coils. In the two central heptad repeats (repeats 3 and 4), in contrast, there are several nonstandard interactions between the coils (Fig. 2, B and C). In repeat 3, the a position is occupied by Asn[181] and the d position by Trp[184] (Fig. 2B). In repeat 4, Asp[188] and Arg[191] occupy these two positions. Asp and Arg occur at the a and d positions, respectively, of coiled coils with less than 1% of their overall frequency in GenBank (16). The effect of placing four disfavored polar and/or bulky residues at both the a and d positions of adjacent heptad repeats is dual. First, the two coils are pushed up to 9 Å apart (fig. S6), versus 6 Å for canonical parallel dimeric coils (17). Second, to avoid steric overlap and electrostatic repulsion, the structure
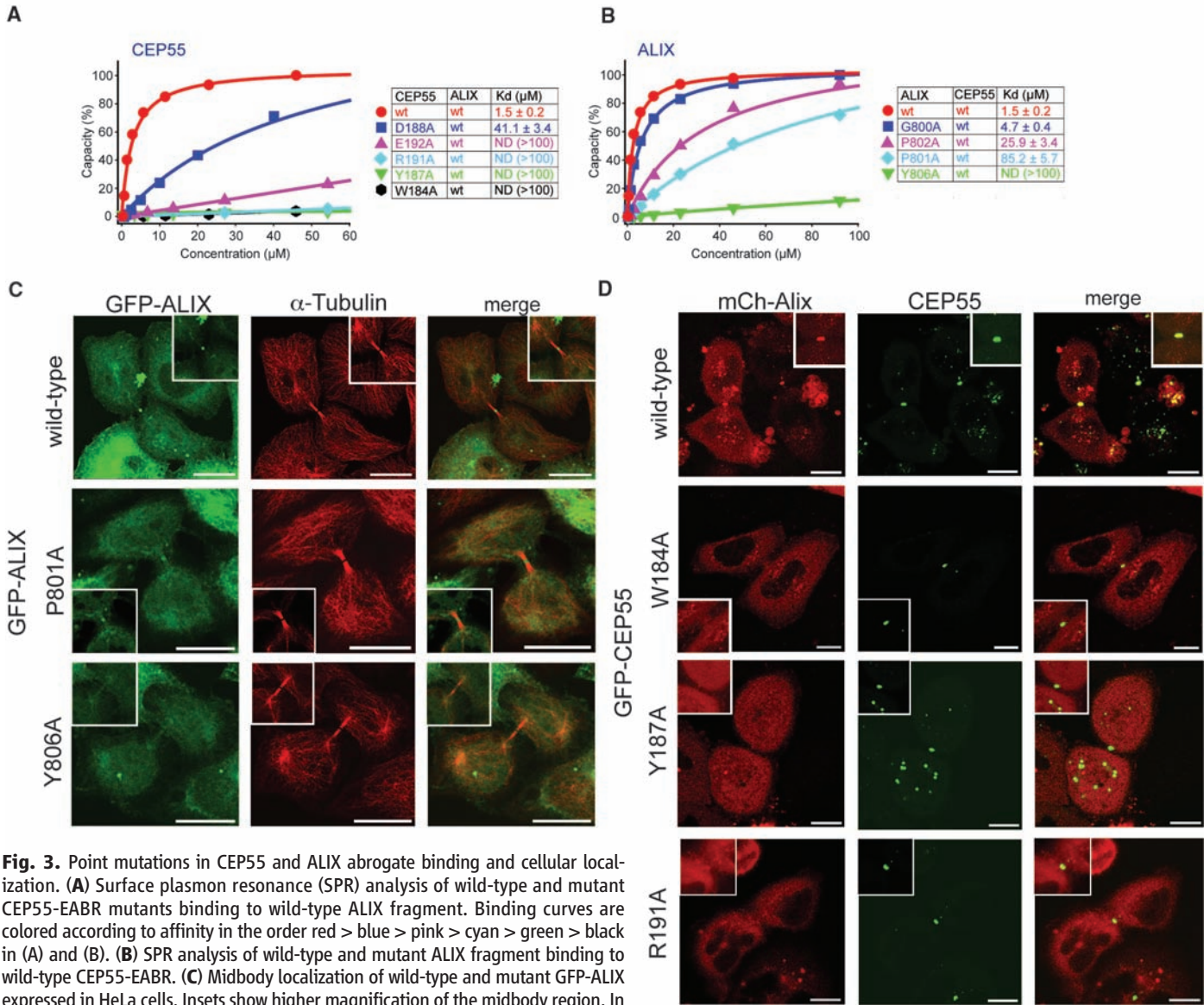

Fig. 3. Point mutations in CEP55 and ALIX abrogate binding and cellular localization. (**A**) Surface plasmon resonance (SPR) analysis of wild-type and mutant CEP55-EABR mutants binding to wild-type ALIX fragment. Binding curves are colored according to affinity in the order red > blue > pink > cyan > green > black in (A) and (B). (**B**) SPR analysis of wild-type and mutant ALIX fragment binding to wild-type CEP55-EABR. (**C**) Midbody localization of wild-type and mutant GFP-ALIX expressed in HeLa cells. Insets show higher magnification of the midbody region. In the middle panels, α-tubulin staining was used to highlight the midbody microtubule structure. (**D**) Live-cell imaging of midbody localization of wild-type mCh-ALIX and wild-type or mutant CEP55 coexpressed in HeLa cells. CEP55 midbody localization was not affected in the mutant (fig. S7). Insets show higher magnification of the midbody region. Scale bars, 10 μm.

becomes asymmetric (Fig. 2C). By pushing apart the two coils in an asymmetric manner, the four noncanonical a- and d-position residues create a single binding site for the ALIX peptide.

The ALIX peptide interacts with CEP55-EABR via its GPP sequence (Gly[800], Pro[801], Pro[802]) and Tyr[806], which together form the GPPX$_3$Y motif. The peptide conformation is kinked between the GPP and Tyr[806], and wraps around the protruding side chain of CEP55 Tyr[187] (Fig. 2, D and E). CEP55 Tyr[187] is essential for the ALIX interaction (Fig. 3A). The GPP sequence makes extensive contacts with CEP55 Trp[184] and Tyr[187] and with the aliphatic portions of the Lys[180] and Gln[183] side chains (Fig. 2, D to G). Mutation of CEP55 residues Trp[184] or Tyr[187] reduces binding to essentially undetectable levels (Fig. 3A). Within the GPP sequence, Pro[801] makes the most extensive contacts of the three residues of the GPP motif, and its mutation to Ala reduces binding by a factor of ~60 (Fig. 3B). The Gly and the second Pro make correspondingly smaller but still substantial contributions to specificity (Fig. 3B). The second major point of contact involves ALIX Tyr[806], which wedges its ring between CEP55 Tyr[187] and Trp[184] and forms a short, strong hydrogen bond between its hydroxyl and the side chain of Glu[192]' (Fig. 2, E and F). Mutation of

Glu[192] reduces binding by a factor of ~30 (Fig. 3A), whereas mutation of ALIX Tyr[806] almost completely abolishes binding (Fig. 3B).

To evaluate the effect of interfering with ALIX-CEP55 interactions on the subcellular localization of ALIX, we tagged full-length ALIX mutants with green fluorescent protein (GFP) and compared their localization to that of wild-type ALIX. Whereas wild-type ALIX strongly localized to midbodies (Fig. 3C, top row) (12, 13), ALIX[P801A], which had weaker binding affinity in vitro, had reduced midbody localization (Fig. 3C, row 2). Notably, ALIX[Y806A], which completely blocks binding in vitro, showed no midbody localization above background (Fig. 3C, bottom row). The magnitude of the effect of mutating the ALIX GPPX$_3$Y motif on localization thus correlates well with the effects on in vitro binding and with the structure.

To further understand the relationship between ALIX and CEP55 in cells, we tested a series of GFP-CEP55 mutants at the corresponding binding residues. Although the localization of CEP55 to midbodies was not affected in any of the mutants (fig. S7), ALIX localization appeared to be impaired. Specifically, cells cotransfected with wild-type mCh-ALIX (mCh, monomeric cherry red fluorescent protein) and any of the

CEP55 mutants W184A, Y187A, and R191A showed severely impaired midbody localization of mCh-ALIX relative to wild-type CEP55 (Fig. 3D). This shows that the integrity of CEP55-EABR is important for ALIX to target to this structure. When mCh-TSG101 was cotransfected with CEP55 mutants (fig. S8), a similar CEP55 dependence on TSG101 midbody localization was observed. Taken together, the cellular results strongly corroborate that the interfacial residues observed in both ALIX and CEP55 are responsible for the physiological localization of ALIX by CEP55. Furthermore, the localization of TSG101 is shown to be controlled in cells by the same key EABR residues in CEP55 as for ALIX.

The ESCRT machinery directs a conserved membrane cleavage reaction that is important in multiple cellular processes. At the endosome, the ESCRTs have a dual function in cargo sorting and membrane budding. ESCRTs are targeted to endosomes by multiple low-affinity ($K_d > 100$ μM) interactions with ubiquitinated membrane proteins and micromolar interactions with 3-phosphoinositides (7–11). Viruses such as HIV-1, in contrast, appear to self-organize into buds and require the ESCRTs for their final scission from the plasma membrane of the host cell (18–20). In viral budding, ESCRT targeting is mediated primarily by micromolar-affinity ($K_d \sim 5$ to 30 μM) interactions with PTAP and YPXL motifs (21) and ESCRT-I (22) and ALIX (23, 24), respectively. ESCRT targeting to the midbody appears more similar to the situation in viral as opposed to endosomal budding, in that a single, highly specific micromolar binary interaction between GPPX$_3$Y motifs and CEP55-EABR is key to recruitment. These observations are consistent with a model in which the ESCRTs have a broad-based modular membrane scission activity targeted via the recognition of short peptide motifs, in addition to their endosome-specific, ubiquitin-directed ability to cluster cargo.

In a working model for cleavage of the membrane neck, ESCRT-I and ALIX recruit ESCRT-III components, which are also found at the midbody (13). ESCRT-III forms a circular array that is an attractive candidate to drive the closure and cleavage of the membrane neck (15). Indeed, an ALIX allele defective in binding the ESCRT-III subunit CHMP4 does not support cytokinesis (14). Both ESCRT-I and ALIX are needed for cytokinesis, at least in HeLa cells (12, 13). Our finding that one CEP55 dimer binds to only one copy of ALIX or ESCRT-I indicates that multiple CEP55 dimers are required for function, which suggests that the nucleation of ESCRT-III assembly occurs at a minimum of two sites. The unexpected finding that the region previously thought to form a hinge between the N-terminal and C-terminal coiled coils is, in fact, itself in a coiled-coil conformation and is probably contiguous with the N-terminal coiled coil provides tight constraints on possible models for the organization of CEP55 within the midbody. A possible model that incorporates the characterization of the CEP55-EABR:ALIX complex and related crystallographic (25–27) and electron

Fig. 4. A model for the organization of CEP55-ESCRT and CEP55-ALIX complexes in the midbody. The model of the N-terminal half of the CEP55 structure docked to the ESCRT-I core (25) and UEV domain (22) and ALIX (26) structures is described in the supporting online material. The crystallized EABR portion of the CEP55 coiled coil is highlighted in red. The structure of the C-terminal domain of the yeast Vps28 subunit of ESCRT-I is shown (28) as a putative binding site for Vps20, the yeast ortholog of the human ESCRT-III subunit CHMP6. The binding site on the Bro1 domain of ALIX for the C-terminal helix (blue) of the CHMP4 subunit of ESCRT-III is shown (27, 29). A schematic of an ESCRT-III circular array (15) is also shown. The width of the membrane neck is not to scale.
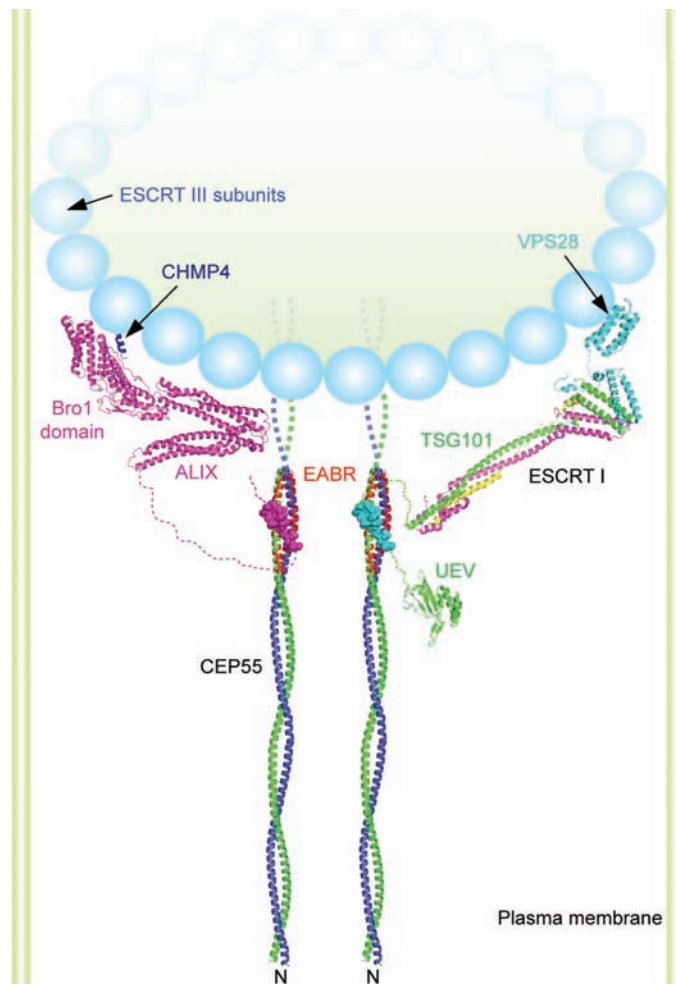
microscopic analyses (*15*) is shown in Fig. 4. Although much remains to be learned about the molecular architecture of the midbody and the precise stereochemistry of cytokinesis, the results and model presented here provide one foothold for furthering such an understanding.

References and Notes

1. M. Glotzer, *Science* **307**, 1735 (2005).
2. F. A. Barr, U. Gruneberg, *Cell* **131**, 847 (2007).
3. R. Prekeris, G. W. Gould, *J. Cell Sci.* **121**, 1569 (2008).
4. W. M. Zhao, A. Seki, G. W. Fang, *Mol. Biol. Cell* **17**, 3881 (2006).
5. I. Martinez-Garay, A. Rustom, H. H. Gerdes, K. Kutsche, *Genomics* **87**, 243 (2006).
6. M. Fabbro *et al.*, *Dev. Cell* **9**, 477 (2005).
7. T. Slagsvold, K. Pattni, L. Malerod, H. Stenmark, *Trends Cell Biol.* **16**, 317 (2006).
8. R. L. Williams, S. Urbe, *Nat. Rev. Mol. Cell Biol.* **8**, 355 (2007).
9. D. P. Nickerson, D. W. Russell, G. Odorizzi, *EMBO Rep.* **8**, 644 (2007).
10. S. Saksena, J. Sun, T. Chu, S. D. Emr, *Trends Biochem. Sci.* **32**, 561 (2007).
11. J. H. Hurley, *Curr. Opin. Cell Biol.* **20**, 4 (2008).
12. J. G. Carlton, J. Martin-Serrano, *Science* **316**, 1908 (2007); published online 6 June 2007 (10.1126/science.1143422).
13. E. Morita *et al.*, *EMBO J.* **26**, 4215 (2007).
14. J. G. Carlton, M. Agromayor, J. Martin-Serrano, *Proc. Natl. Acad. Sci. U.S.A.* **105**, 10541 (2008).
15. P. I. Hanson, R. Roth, Y. Lin, J. E. Heuser, *J. Cell Biol.* **180**, 389 (2008).
16. A. Lupas, M. Van Dyke, J. Stock, *Science* **252**, 1162 (1991).
17. E. K. O'Shea, J. D. Klemm, P. S. Kim, T. Alber, *Science* **254**, 539 (1991).
18. E. Morita, W. I. Sundquist, *Annu. Rev. Cell Dev. Biol.* **20**, 395 (2004).
19. P. D. Bieniasz, *Virology* **344**, 55 (2006).
20. K. Fujii, J. H. Hurley, E. O. Freed, *Nat. Rev. Microbiol.* **5**, 912 (2007).
21. Single-letter abbreviations for amino acid residues: A, Ala; C, Cys; D, Asp; E, Glu; F, Phe; G, Gly; H, His; I, Ile; K, Lys; L, Leu; M, Met; N, Asn; P, Pro; Q, Gln; R, Arg; S, Ser; T, Thr; V, Val; W, Trp; Y, Tyr; X, any amino acid.
22. O. Pornillos, S. L. Alam, D. R. Davis, W. I. Sundquist, *Nat. Struct. Biol.* **9**, 812 (2002).
23. U. M. Munshi, J. Kim, K. Nagashima, J. H. Hurley, E. O. Freed, *J. Biol. Chem.* **282**, 3847 (2007).
24. Q. Zhai *et al.*, *Nat. Struct. Mol. Biol.* **15**, 43 (2008).
25. M. S. Kostelansky *et al.*, *Cell* **129**, 485 (2007).
26. R. D. Fisher *et al.*, *Cell* **128**, 841 (2007).
27. J. Mccullough, R. D. Fisher, F. G. Whitby, W. I. Sundquist, C. P. Hill, *Proc. Natl. Acad. Sci. U.S.A.* **105**, 7687 (2008).
28. E. Pineda-Molina *et al.*, *Traffic* **7**, 1007 (2006).
29. J. Kim *et al.*, *Dev. Cell* **8**, 937 (2005).
30. We thank B. Beach for generating DNA constructs, E. Freed and K. Kutsche for providing DNAs, T. Alber for discussions, and the staff of SER-CAT for user support at the Advanced Photon Source (APS). Use of the APS was supported by the U.S. Department of Energy, Basic Energy Sciences, Office of Science, under contract W-31-109-Eng-38. Supported by NIH intramural support, NIDDK (J.H.H.), NICHD (J.L.), and IATAP (J.H.H. and J.L.). Crystallographic coordinates have been deposited in the RCSB Protein Data Bank with accession number 3E1R.

Functional Traits and Niche-Based Tree Community Assembly in an Amazonian Forest

Nathan J. B. Kraft,[1] Renato Valencia,[2] David D. Ackerly[1]

It is debated whether species-level differences in ecological strategy, which play a key role in much of coexistence theory, are important in structuring highly diverse communities. We examined the co-occurrence patterns of over 1100 tree species in a 25-hectare Amazonian forest plot in relation to field-measured functional traits. Using a null model approach, we show that co-occurring trees are often less ecologically similar than a niche-free (neutral) model predicts. Furthermore, we find evidence for processes that simultaneously drive convergence and divergence in key aspects of plant strategy, suggesting that at least two distinct niche-based processes are occurring. Our results show that strategy differentiation among species contributes to the maintenance of diversity in one of the most diverse tropical forests in the world.

Explaining the high species diversity of moist tropical forests has proved an enduring challenge to ecologists and has inspired many theories of species coexistence and much debate (*1–3*). Current coexistence theories can be divided into two categories: those that invoke a role for meaningful differences in the ecological strategy (niche) of co-occurring species (*2–5*), and those that rely on dispersal and stochastic demographic processes that explicitly assume the equivalent per capita fitness of species (*1*). The latter, termed neutral theory, was initially developed to explain coexistence in diverse tropical forests (*1*), where it seemed implausible that each tree species occupied a unique niche, although it can be applied to a range of communities.

Few large-scale tests of coexistence theories in tropical forests have explicitly examined the ecological strategy of co-occurring species, in part because of difficulties in identifying more than a few discrete plant strategies (such as shade-tolerant, light-demanding pioneer, etc.) (*6*). Recent advances in functional ecology now permit a more precise quantification of woody plant strategy along a number of continuous, often orthogonal, axes of variation related to resource acquisition strategy, regeneration niche, environmental tolerance, and life history (*7–10*), opening the door for previously intractable analyses.

Here we present a critical test of neutral and niche-based coexistence theories in one of the most diverse tropical forest plots in the world. The stochastic processes associated with neutral theory assume the equivalence of all individuals, and therefore species, with the result that species co-occurrence patterns should be random with respect to ecological strategy (*1, 11*). We tested for two niche-based alternatives: (i) that co-occurring species converge in strategy because of establishment and/or survival barriers imposed by the abiotic environment ("environmental filtering") (*4, 12, 13*); and (ii) that co-occurring species diverge in strategy as predicted by classic coexistence theory ("niche differentiation") (*5, 14*). The latter pattern may occur as a result of competition or of enemy-mediated density dependence (*15*) if plant susceptibility (*16*) and overall plant strategy are phylogenetically conserved. A strength of our approach is that we are able to test for both processes (*17*), because environmental filtering should limit the range of strategies found in a community (*12, 17*), whereas niche differentiation should spread individuals evenly along strategy axes (*14, 17*). These two features of community-trait distributions can be assessed sequentially.

We tested these predictions in the Yasuní Forest Dynamics Plot (FDP) in eastern Ecuador, a 25-ha plot containing over 150,000 mapped trees ≥1 cm in diameter at breast height (dbh) from over 1100 species (*18*). The ecological strategy for each species was quantified with field-measured estimates of specific leaf area (SLA, leaf area divided by dry mass), leaf nitrogen concentration, leaf size, seed mass, and maximum dbh (used here as a proxy for maximum height), as well as published estimates of wood density (*19, 20*). We combined this trait information with species co-occurrence data to develop estimates of the community-trait distribution at the 20-by-20–m ("quadrat") scale. Metrics of community-trait structure sensitive to environmental filtering and niche differentiation were compared to a null expectation. We generated our null expectation by creating random communities of equal richness by drawing species from the entire plot weighted by their plot-wide occurrence, irrespective of trait values (*20*).

We predict that if habitat filtering is occurring at the quadrat scale, the range of observed trait

[1]Department of Integrative Biology, University of California, Berkeley, CA 94720, USA. [2]Laboratorio de Ecología de Plantas, Escuela de Ciencias Biológicas, Pontificia Universidad Católica del Ecuador, Aptado, 17-01-2184, Quito, Ecuador.